

Chapter 30 in Cardiac Electrophysiology: From Cell To Bedside

Edition 4

Editors: Douglas Zipes and Jose Jalife

**Three Dimensional Propagation in
Mathematical Models: Integrative Model of
the Mouse Heart**

Craig S Henriquez¹, Joseph V. Tranquillo¹, David Weinstein²,

Edward Hsu¹, Christopher R. Johnson²

¹Department of Biomedical Engineering, Duke University

²Department of Computer Science, Scientific and Computing Institute, University of Utah

Correspondence:

Craig Henriquez, PhD
136 Hudson Hall, Department of Biomedical Engineering
PO Box 90281
Duke University
Durham NC 27708
Phone: 919-660-5168
Fax: 919-684-4488
Email: ch@duke.edu

Introduction

Computer models have been used to study cardiac conduction since the late 1970's [1]. At that time, computational power limited investigations to very simple geometries corresponding to single fibers or monolayer sheets of cells. With the evolution of computer technologies, computational models of the heart have become three-dimensional and increasingly more realistic [2-4], allowing a wider range of investigations to elucidate fundamental relationships of a set of biophysical parameters and the underlying potential distributions and current flow.

Despite the considerable advances, there are relatively few models that integrate knowledge and data from the ion-channel to the organ level. One reason for this is a simulation of wavefront propagation in the whole heart at the resolution of a single cell quickly exceeds the computational capacity of the typical computer. We recently estimated the computational cost of simulating a single beat on a model of the human heart at "cellular" spatial resolution [5]. The volume of heart muscle is roughly 225 cm^3 . To simulate the flow of current, we must first subdivide this volume into a computational grid of roughly similar sized elements. For box elements of volume $(0.01 \text{ cm})^3$, a grid of 225×10^6 nodes is required. For each one of nodes we must assign a local conductivity tensor (set of conductivities representing the fiber properties), a set of ion currents and some adjustable parameters. Assuming 50 numbers are associated with each node to define this information, 50 numbers \times 4 Bytes/ number \times 225×10^6 or 45 GBytes are needed just to hold the model in memory. To simulate an arrhythmia of only 10 sec with a time resolution of $10 \mu\text{s}$ (needed to resolve the fast kinetics of the sodium channel), these 10×10^{10} numbers would have to be evolved over 10^6 time steps. Consequently, a simulation of electrodynamics using an integrative model of the human heart at near cellular resolution is not very practical or even tractable, leading many to consider smaller hearts [2,3] where more is known about both the anatomy and membrane kinetics, given the wide range of experimental methods available to interrogate the electrophysiology in vitro.

Unfortunately, the nature of the action potentials and wavefront dynamics in these small animal hearts can be very different than in human hearts, owing in part to the marked differences in heart size, wall thickness, ion channel type and distribution. Furthermore, the differences in size and membrane kinetics are expected to impact the spatial scales over which certain types of heterogeneity can be manifested, confounding the ability to derive meaningful mechanisms of clinical arrhythmogenesis.

The challenge of relating phenomena in small hearts to that found in larger hearts has become more important given the increase use of the mouse as a model of human cardiovascular disease. Because of the relative ease of manipulating the genome, there are now mouse models of long QT syndrome [6,7], hypertrophy [8,9] and regional ischemia [10] and other clinically relevant conditions [12]. In the human heart, it is widely believed that many disease states lead to an increased probability of arrhythmia by increasing the heterogeneity in the structure of cardiac tissue and/or the expression of ion channel proteins. Because of the vastly different geometries and membrane kinetics, computer models are needed to derive the appropriate scaling laws and by doing so, help to elucidate the relationship between the mouse and human electrophysiology.

A step toward this goal, is to create a computational model of wavefront conduction in the mouse heart that can yield data that can be related to clinical measurements such as including surface and transmural electrograms, Monophasic Action Potential (MAP) recording, and body surface ECG. To accomplish this, the model of the mouse heart will need to include descriptions of the ventricular/atrial geometry, the local fiber orientation, material properties of the intracellular and extracellular spaces and the spatial distribution of the ion channels governing the activation and recovery processes. Ideally, these properties should be tunable over a range of pathological states to interpret a variety of experimental findings in the mouse heart.

In this chapter, we present an integrative model of the mouse heart that combines a detailed description of the ion channel dynamics with a realistic description of the ventricular

geometry and fiber architecture. In addition, we present a paradigm for the rapid construction of preparation specific models of the mouse heart to explore normal and abnormal wavefront propagation. The paradigm combines semi-automated segmentation of magnetic resonance datasets to obtain the heart geometry and the local fiber orientation with advanced computational methods to solve the underlying equations of reaction and diffusion. We demonstrate the utility of this approach by simulating the activation and recovery patterns for a simple paced beat and generating signals that can be compared directly to data obtained from optical or electrical mapping. The results show that despite its small size, an integrative, three-dimensional model of the mouse heart can be used as a testbed to explore many fundamental phenomena of propagation and extracellular fields that are observed in larger hearts

Methods

Diffusion Tensor Imaging

The first step toward creating a computational model of the heart is to obtain an adequate representation of both the ventricular geometry and the fiber architecture. Histological, sectioning methods have long been the standard for acquiring this information. LeGrice et al. used the histological data to create a finite element mesh of the canine ventricles [13]. Vetter and McCulloch used an analogous approach to create a model of the rabbit [2]. Unfortunately, the data gathering and reconstruction phases of serial sectioning methods are very time-consuming, leading to only a few stereotypic whole heart models.

An alternative to sectioning for acquiring fiber directions is the use of MRI diffusion tensor imaging (DTI) methods [14] DTI exploits the dependence of the molecular diffusion of water in the tissue microstructure to provide estimates of the local fiber structure. Random translational motion, such as diffusion, has been shown to cause an irreversible loss of coherence and thus attenuates the MR signal. The signal attenuation in cardiac tissue can be expressed as:

$$A(TE) = \exp \left[-(\mathbf{v}^T \boldsymbol{\Sigma} \mathbf{v}) \lambda^2 \int_0^{TE} \left(\int_0^t G(\tau) d\tau \right)^2 dt \right] \quad (1)$$

where $t = TE$ is the time of echo, G is a time-varying magnetic field gradient vector, λ is the spin gyromagnetic constant and

$$\mathbf{v}^T = [g_\xi g_\eta g_\zeta] \quad \boldsymbol{\Sigma} = \begin{bmatrix} D_\xi & 0 & 0 \\ 0 & D_\eta & 0 \\ 0 & 0 & D_\zeta \end{bmatrix} \quad (2)$$

The term $\lambda^2 \int_0^{TE} \left(\int_0^t G(\tau) d\tau \right)^2 dt$ is a known experimental parameter that depends on the

echo sequence. The scalar quantity $\mathbf{v}^T \boldsymbol{\Sigma} \mathbf{v}$ is equal to the apparent diffusion coefficient (ADC), which is defined in terms of the laboratory coordinates. The linear transform $\mathbf{v} = \mathbf{U} \mathbf{g}$ (where \mathbf{U} is an orthonormal matrix) transforms \mathbf{v} to the global coordinate system

$$ADC = \mathbf{g}^T \cdot \mathbf{U}^T \boldsymbol{\Sigma} \mathbf{U} \cdot \mathbf{g} \quad (3)$$

From ADC , eigenvalues ($\boldsymbol{\Sigma}$) and eigenvectors (\mathbf{U}) can be computed such that $\mathbf{D} = \mathbf{U}^T \boldsymbol{\Sigma} \mathbf{U}$. The row of \mathbf{U} corresponding to the largest eigenvalue is taken to be the primary fiber direction. Similarly, the secondary fiber direction is taken to be the row of \mathbf{U} corresponding to the second largest eigenvalue. Thus the elements $u_{1..3}$ of \mathbf{U} are found experimentally.

Our group [15] was among the first to show quantitatively that the DTI estimates of fiber orientation in small sections of heart tissue compared well with those measured using standard histology. Socolan et al. [16] used DTI to obtain the 3D fiber structure of the rabbit heart and also found good correspondence to histological measurements. The relative ease of data collection

using DTI versus histology makes it an attractive method to follow morphometric changes through the course of an interventional treatment.

Reaction-Diffusion Model

Once the geometry and fiber directions are obtained, the next step is to create a *stiffness* matrix that contains the information on the geometry and material properties. Cardiac tissue can be viewed as an interconnected mesh of myocytes, collagen and vasculature in which the myocytes are coupled through a conductive intracellular space and surrounded by an interstitial space. The bidomain model was developed to represent cardiac tissue as a syncytium [17]. In the bidomain framework, the intracellular and interstitial spaces are considered to be uniformly continuous. For convenience, quantities associated with the intracellular (i) and interstitial (e) spaces are defined over the entire tissue volume. In tissue, current can only pass from one region to the other through the membrane. In the bidomain model, the transmembrane current is volume averaged and is defined at each point [18]. The bidomain equations are given as:

$$\nabla \cdot (\mathbf{D}_i + \mathbf{D}_e)\phi_e = -\nabla \cdot (\mathbf{D}_i \nabla V_m) \quad (4)$$

$$\nabla \cdot (\mathbf{D}_i \nabla V_m) + \nabla \cdot (\mathbf{D}_e \nabla \phi_e) = -\beta I_m \quad (5)$$

where V_m and ϕ_e are the transmembrane and extracellular potentials, respectively

and $\beta = \frac{2\pi a}{\pi a^2 / f_i} = \frac{2f_i}{a}$ is the surface to volume ratio, where f_i is the fraction of intracellular

space and a is the cell radius. The transmembrane current density, I_m , is composed of a capacitive and an ionic current, namely

$$I_m = C_m \frac{dV_m}{dt} + I_{ion} \quad (6)$$

In the most general case where fiber orientation is not constant, $\mathbf{D}_{i,e}$ becomes a function of position and is assigned separately to each point in both the intracellular and interstitial domains [19].

The bidomain model can be extended to simulate the possible shunting effects of a blood bath or other conductive medium by assuming an adjoining volume conductor in which the potentials and currents satisfy Laplace's equation. At the tissue/air or bath/air boundaries in the intracellular and extracellular spaces, the boundary conditions are no current flux. At the tissue/bath boundaries, the intracellular space is sealed (no flux) while the current and potential are continuous across the boundary in the extracellular space [20]. To obtain a unique solution, the extracellular potential at some point in the domain is set bath to $0V$ to act as the ground.

Numerical Discretization of the Diffusion Matrix

Analytic solutions to the bidomain equations are unavailable in all but the most trivial cases. To solve more realistic problems, a numerical approach must be used. The most common numerical scheme for solving this system of equations is the finite difference (FD) method. This method, however, is best suited to regular geometries. The finite element method (FEM) is the preferred scheme to deal with complicated geometries, but it is less intuitive than FD. An alternative to FEM is the vertex-centered finite volume (FV) method [21]. FV enforces local current conservation and the resulting grid can be interpreted as a lattice of interconnected resistors. In addition, the method naturally enforces no flux boundary conditions, eliminating the need for ghost nodes or other tricks that have plagued finite difference methods for non-rectangular and non-uniformly anisotropic domains. Penland et al. provide a detailed description of the FV method and its application to general, three-dimensional anisotropic cardiac tissue [22].

Ionic Currents

The ionic current in equation 6 is the sum of individual currents flowing across the cell membrane.

$$I_{ion} = \sum_{x=1}^n I_x \quad (7)$$

Generally, I_x is a function of the transmembrane voltage and a non-linear function of some number of state variables representing the gates that modulate current flow, given by

$$I_x = G_x \left(\prod_{p=1}^m z_p^q \right) (V_m - E_x) \quad (8)$$

where z_p is the average state of a given channel ($Closed = 0 \leq z \leq 1 = Open$), q is typically an integer exponent, G_x is the maximum conductance and E_x is the reversal potential for I_x .

The channels themselves are governed by equations of the form

$$\frac{dz}{dt} = \alpha_z(V_m)(1-z) + \beta_z(V_m)z \quad (9)$$

where α_z and β_z are rate constants that are generally dependent on V_m . Alternatively, more detailed descriptions of gating behavior are available in the form of multi-state Markov models, which can facilitate the representation of effects of certain genetic mutations [23].

The specifics of the ionic currents and thus action potential shape depend greatly on species and the location within a given heart. For example, in the mouse heart the transient outward current (I_{to}) is the dominate repolarization current rather than the rapid (I_{kr}) and slow (I_{ks}) repolarization currents that tend to dominate the repolarization phase of the cardiac action potential of larger mammals [24]. The specific distribution of the channels can lead to intrinsic changes in action potential duration throughout the myocardium [25]. The marked differences in the timecourse of the murine cardiac action potential compared to the human cardiac action

potential has raised some questions about the utility of the mouse as a model system of clinical electrophysiological dysfunction.

While no mouse membrane model exists, Pandit et al. recently published a detailed model of the rat myocyte action potential [26]. We have chosen to modify the Pandit model by increasing the upstroke velocity (by increasing the maximum sodium conductance g_{Na} to $1.5mS/cm$) to more closely match experimental findings for the mouse [25].

Model Construction

An intact mouse heart (C57BL/6J strain, Jackson Laboratory, Bar Harbor, Me) was fixed in formalin and scanned using a 1 cm-diameter loop-gap RF coil on a 7.1 T MRI microscope in a short axis view. To minimize displacement, the heart was placed in a centrifuge tube, producing some distortion of the geometry. Three-dimensional standard spin-echo diffusion-weighted images (10 x 10 x 12.5 mm FOV, 500 ms TR, 12.6 ms TE, 3.5 ms-duration half-sine diffusion encoding pulses, 6.3 ms pulse separation) were acquired. The reduced encoding DTI dataset consisted of one full-encoding, high-resolution (128 x 128 x 128 matrix size) non-diffusion-weighted image, and 12 reduced-encoded (128 x 64 x 64) images encoded in each of an optimized set of 12 diffusion-sensitizing directions [5]. Diffusion weighted images were reconstructed to full-encoding matrix size via a modified keyhole method with zeroth order intensity correction. To reduce noise, adaptive Wiener filtering was applied to each image.

Since the MRI data set is a cube of data containing cardiac tissue and non-cardiac tissue, a method was developed to differentiate the two volumes. The raw DT MRI 13-channel data was converted into linear tensors using a non-linear least-squares fitting algorithm [5]. Voxels with low diffusion signals corresponded to non-cardiac tissue (background and blood bath), and were masked out during the least-squares fitting. The non-masked voxels were decomposed into primary, secondary, and tertiary fiber orientations using a standard eigen-decomposition. This

segmented, decomposed data, served as the input into BioPSE software system (Scientific Computing and Imaging Institute, University of Utah) in order to construct the finite volume mesh and corresponding stiffness matrices [27].

To complete the mesh generation, a random seed was placed at a known cardiac node and a flood fill algorithm was used to determine all nodes belonging to the cardiac set. The same procedure was used in the left and right ventricular cavities to identify the blood bath set. All nodes not reached by the three flood fills were eliminated. Due to the node elimination process, some elements were incomplete. Nodes belonging to incomplete elements were eliminated and the remaining nodes were renumbered.

Tissue Properties

The tissue was assumed to be anisotropic with the cross fiber properties to be the same within sheets and across sheets (i.e. transversely isotropic). The following bidomain conductivities were assigned along fibers: $g_{it} = 5.0$ mS/cm, $g_{et} = 4.0$ mS/cm; the following were assigned across fibers: $g_{it} = 0.5$ mS/cm, $g_{et} = 1.33$ mS/cm. The surface to volume ratio was 1666 cm⁻¹, corresponding to a cell radius of 8.4 microns and a fraction of intracellular space of 0.7.

Numerical Methods

Equations 4 and 5 were solved numerically using a semi-Implicit Crank-Nicholson scheme where the equations of the state variables for I_{ion} in Eq. 6 were updated with forward Euler method. A fixed timestep of 2.0 μ s was used. The extracellular ground was placed in the RV blood cavity. The Cuthill-McKee Algorithm was used to minimize the bandwidth of the matrix. The resulting system of equations was solved using an iterative Jacobi preconditioned GMRES algorithm with a tolerance of 10^{-4} mV. All simulations were performed using the custom software tool CARDIOWAVE (Duke University) [28] developed in our laboratory. The modular software is

designed to run on multiple processors. All simulations were executed on an IBM SP Power 3 System at the North Carolina Supercomputing Center. 100 msec of simulated activity required 6 hours on 11 processors.

Results

When performing a DTI scan, a non-diffusion weighted image is usually acquired to obtain the geometry, facilitating subsequent registration. Figure 1A shows a volume rendering of portion of the fixed mouse heart geometry used to create the computational mesh. Figure 1B shows a rendering of the computational grid formed from segmentation of the DTI data. Each element is a regular cube with dimensions of approximately $75 \times 75 \times 75$ microns. At this resolution, the volume of the mouse heart comprises 225,236 nodes. The ventricular cavity is also discretized into 793 nodes so a blood bath can be incorporated for bidomain computations. The DTI data gives a local tensor at each voxel. The eigenvector associated with the largest eigenvalue has a direction that is aligned with the fiber direction. The surface fiber directions are shown on the geometry of Figure 1B as small white lines. The surface fibers run obliquely from apex to base on a portion of LV free wall and away from the septum they tend to run circumferentially around the heart. On the endocardial surface the fibers tend to align more vertically from apex to base. Note that unlike the mathematical description used by Legrice et al. [13] and Vetter and McCulloch [2], the fiber directions show significant local variation. Some of this is due to normal physiological variation, but some is due to the preparation of the heart and to processing artifacts arising from small tissue displacements that occur during then scan. The fibers through some portions of the wall reveal a surprisingly smooth rotation, similar to that found in the hearts larger mammals. The rotation of 80-90 degrees, however, is less than the 110-130 degrees found in larger hearts, although the rate of rotation is considerably faster, since the LV has an average thickness of approximately 1.5 mm and the RV has an average thickness of approximately 0.6 mm.. Three

projections of the fibers, uniformly sampled across the RV and LV, are shown in Figure 2, in two separate views.

To study the activation and recovery, a stimulus was applied on the epicardial surface of the LV to simulate an ectopic beat. Figure 3 shows the transmembrane (V_m) and extracellular (Φ_e) potential distribution on the LV surface 0.5 msec (top row), 6.5 msec (second row), 8.5 msec (third row) and 10.5 msec (bottom row) after the stimulus onset. The distribution at 0.5 msec is during the application of the stimulus. In all images, light areas denote depolarized or positive potential, where darker regions denote hyperpolarized or negative potentials. At 0.5 msec, the transmembrane potential map reveals a small virtual cathode, by a characterized depolarized region flanked by two hyperpolarized regions [29]. The hyperpolarization is, however, very small (less than 0.5 mV) for the stimulus strength used. After the stimulus the wavefront propagates outward as an ellipsoidal front. For the assigned properties, the propagation velocity is approximately 68 cm/sec along fibers and 34 cm/sec across fibers. Both the pattern and conduction velocities compare well to that observed by Nygren et al. for the mouse using voltage sensitive dyes [30]. The extracellular potential distribution is characterized by a central negative region with two positive maxima that are roughly aligned with the surface fiber direction. This classical pattern is consistent with that first described by Taccardi et al. [31] in canine hearts and later by Macchi et al in rat hearts [32]. Because the mouse LV wall is thinner than the canine LV wall, however, there much less rotation in these patterns as the front propagates transmurally, compared to the canine heart [33].

Figure 4A shows the activation map that is obtained by tracking the time the upstroke reaches -60 mV at every point. For the given pacing site, the entire heart activates in approximately 24 msec. Figure 4B shows the recovery map, obtained by tracking the point at which the recovery tail reached -60 mV. Note that the recovery map has a bullseye pattern near the

stimulus. This region recovers from outside to inside, so that stimulus site is the last to recover [34]. The remainder of the heart recovers in the same direction as activation. Because of the small heart size and strong electrotonic effects, the recovery is completed within 6 msec (62 msec to 68 msec). Note that the recovery map is broader and less anisotropic than the activation map, due in part to the longer effective length constant during repolarization. Finally, the difference in the activation and recovery patterns is the APD distribution (Figure 4C). The APD range is 43.2 msec to 63.9 msec with the longest APD near the stimulus site. It is important to emphasize that these patterns are observed in the model because we assumed

One advantage of computational modeling is the ability to relate measurements such as electrograms with transmembrane potentials and currents at high spatial resolution in the same preparation. Figure 5 shows two representative surface transmembrane potential signals and the corresponding electrograms at the sites along and across fibers. As has been reported in larger hearts, the amplitude of the electrograms across fibers is smaller and the shape is less symmetric than the electrograms along fibers. Both electrograms exhibit a prominent J wave, associated with the rapid early phase of repolarization and a slight T wave associated with the late phase of repolarization. Another significant advantage of the model is that information can be obtained in three dimensions. Figure 6 shows the transmembrane potentials and electrograms at five sites across the wall near the stimulus site. The times of the maximum negative deflection in the electrograms and the maximum rate of rise of the upstroke are coincident and are slightly shifted to the right as the front propagates from epicardium to endocardium. Note that the electrograms tend to increase in amplitude across the wall due, in part, to a reduction in front curvature.

Discussion

It has long been recognized that three-dimensional models of the whole heart are needed to study many types of normal conduction and reentrant arrhythmias that cannot be reproduced in models of small sections of tissue. Early whole heart models used cellular automaton algorithms with isotropic properties [35,36]. Later models incorporated realistic anatomy and fiber orientations, but relied on simplified FitzHugh-Nagumo kinetics or variants of the automaton approach to obtain reasonable simulation times [37-39]. It has only been within the last couple of years that investigators have attempted to create and use three-dimensional models that are truly integrative, combining both realistic representations of anatomy and tissue properties with realistic models of ion fluxes [3,4,40]. To achieve an integrative model, however, the heart sizes are generally smaller than human size and the spatial resolution is significantly larger than a single cell, in some cases compromising numerical accuracy. In this chapter, we demonstrated an approach for creating a preparation specific model of wavefront propagation in the mouse heart at near cellular resolution, using geometry and fiber data obtained directly from MRI images. By combining advanced visualization and analysis tools like BioPSE [27] with efficient, parallel computational algorithms such as those used in CARDIOWAVE [28], the approach can be extended straightforwardly to the human heart.

The differences in the cardiac dimensions of the mouse and human heart are striking. The typical adult mouse heart weighs between 150 and 175 mg [12]. In contrast, the adult human heart weighs approximately 280,000 mg. The mouse heart used in this study had an average LV wall thickness of approximately 1.5 mm, and an average RV wall thickness of approximately 0.6 mm. These dimensions are roughly an order of magnitude smaller than the human heart. In fact, the RV murine heart wall is only about 3 or 4 resting length constants for current flow, significantly impacting transmural activation in the heart. Perhaps the most compelling fact is that the number of cells in the mouse heart (10×10^6 myocytes) is within that used for several large-scale models of

heart dynamics (41). Thus it is conceivable, with modern day computers, to simulate tens of beats in a model of the entire mouse heart at cellular resolution, with a physiologically realistic model of the action potential.

While there have been some investigations to quantify the fiber architecture in mouse heart using serial sectioning methods, this study represents the first attempt to obtain this information using non-destructive diffusion tensor imaging. McLean and Prothero reported that the heart wall was like a "sandwich," in which the myofibers in the middle layer run mainly circumferentially, whereas those in the inner and outer layers run parallel or oblique to the apical-basal axis, a variant of the classical model of the myofiber pattern [42]. While DTI imaging (albeit on only one heart) yielded similar patterns for the gross fiber directions as described by McLean and Prothero, the transmural rotation of the fibers in some portions of the LV free wall was smoother than that found using histology. The differences in findings could be attributed to the techniques themselves or to difference in hearts (e.g. age, strain, etc). More study is required to resolve this discrepancy.

It is important to emphasize that the data was obtained from an explanted heart fixed in formalin. Although there are challenges in appropriately pressure loading the heart to achieve a normal shape, the use of fixation allows longer imaging times, higher spatial resolution and better signal to noise than that obtained in vivo. The use of fixation also eliminates the possible corruption of the signal from perfusion and does not appear to affect the estimates of fiber orientation [43]. While diffusion tensor imaging was used here to obtain the orientation of fibers along the long axis, there is some evidence to suggest that the method can also provide estimates of the sheet structure that has been hypothesized to exist based on histology. For the simulations presented, the fiber data was not interpolated from a small subsample of fiber measurements. Instead, the fiber estimates obtained from the DT images for each voxel was used. Because of the challenges of preparing a heart of this small size for scanning, some artifacts in the fiber estimates arose at the myocardial borders likely due to small shifts/deformations of the heart caused by

diffusion induced eddy currents in the scanner. Some of these artifacts may be corrected by registering the images acquired for different gradient directions before estimating the tensors or eliminating fiber estimate that fall below some threshold of anisotropy ratio. These schemes are currently being tested to improve the model construction process.

Because of the small heart size, the computational grid that is generated after processing the MRI data is at a fine spatial resolution, but the surfaces of the grid are not smooth. The advantage of using a stairstep mesh rather than a boundary fitted mesh is that it can be created very rapidly and it avoids some of the numerical issues associated with adjacent element of different sizes. Using the FV scheme, a stiffness matrix can be created directly using the MRI voxels as elements. This approach makes it possible to create preparation specific models for each heart used in a given study to help explain any possible heart to heart variation in the electrophysiology.

The small heart size also enabled us, for the first time, to use a fully coupled bidomain formulation in a integrative model of the whole heart. With this model, both the transmembrane and extracellular potentials could be computed for an entire paced beat. While not yet completely experimentally validated, the patterns of transmembrane potential are qualitatively similar to those recorded optically by Nygren et al. [31] in the mouse heart and the extracellular potential patterns are consistent with those measured by Macchi et al. in the rat [32]. Perhaps more importantly, the patterns are similar to those observed in larger hearts, suggesting that the mouse heart and computer models based on the mouse geometry can be used to study both wavefront propagation and fundamental source-field relationships over a wide range of conditions that can be potentially achieved through genetic manipulation.

The ability to experimentally manipulate the genome makes the mouse an excellent experimental system to probe the genetic aspects of electrical dysfunction. It is becoming

increasingly clear, however, that arrhythmogenesis is not simply explained by the presence of a certain gene or the individual proteins that the gene codes for, but rather how the proteins interact in some signaling pathway to create a substrate for propagation failure [44]. This arrhythmogenic substrate usually involves changes in both the structure (how the cells are connected) and the distribution and kinetics of the ion channels [45,46]. By using simulation, it will eventually be possible to compute these protein interactions first in an integrative model to test a hypothesis in silico and then design the appropriate experiment or transgenic mouse to investigate a clinically relevant condition.

As noted earlier, an important challenge to overcome in using the mouse heart is to relate the phenomena associated with certain protein interactions at the small scale to those expected in the larger human heart. While certain aspects are still beyond our reach, computer models will likely play a major role in providing the linkages at these disparate scales. As always, investigators will need to find the right level of complexity of the model that will allow them to gain insight into the phenomena of interest and to determine the next avenue for feasible experimental inquiry. As demonstrated in this study, the models should be able to generate output in such a way that information that can be measured experimentally can be related to information that cannot. For example, it is possible to measure electrograms or fluorescence indicative of transmembrane potential at multiple sites in the heart, but not the individual ionic currents. An integrative model that links these two pieces of data can help unmask the molecular basis of a certain arrhythmia. By combining optical imaging methods and MRI techniques, it may soon be possible to map the distribution of gene expression onto the three-dimensional geometry and incorporate this information into a computer model of transgenic mouse heart [47,48]. This type of information will be critical to fully understanding the kind of protein interactions that promote arrhythmogenicity. Finally, by adhering to the philosophy of modeling what can be measured, integrative three-dimensional models of the heart using realistic ion channel dynamics can be joined with models of the current flow in the torso to compute the ECG, providing a computational

framework to investigate electrophysiology of the heart from the level of the protein to routine clinical observation.

References

1. Henriquez, CS, Papazoglou, AA: Using computer models to understand the roles of tissue structure and membrane dynamics in arrhythmogenesis. *Proc IEEE* 84:334-354,1996.
2. Vetter FJ, McCulloch AD: Three-dimensional analysis of regional cardiac function: a model of rabbit ventricular anatomy. *Prog Biophys Mol Biol.* 69:157–83, 1998.
3. Trayanova, N, Eason, J, Aguel, F: Computer simulations of cardiac defibrillation: a look inside the heart. *Comput Visual Sci* 4:259-270, 2002
4. Harrild DM, Henriquez CS: A computer model of normal conduction in the human atria, *Circ Res*, 87:E25-E36, 2000.
5. Cherry EM, Greenside HS, Henriquez CS: A space-time adaptive method for simulating complex cardiac dynamics. *Phys Rev Let.* 84:1343-6, 2000.
6. London B, Jeron A, Zhou J, Buckett P, Han X, Mitchell GF, Koren G: Long QT and ventricular arrhythmias in transgenic mice expressing the N terminus and first transmembrane segment of a voltage-gated potassium channel. *Proc Nat Acad Sci* 95:2926-31, 1998.
7. Mitchell GF, Jeron A, Koren G: Measurement of heart rate and QT interval in the conscious mouse. *Am J Physiol, Heart Circ Physio.* 274: H747-H751, 1998.

8. Gottshall KR, Hunter JJ, Tanaka N, Dalton N, Becker KD, Ross J Jr., Chien KR: Ras-dependent pathways induce obstructive hypertrophy in echo-selected transgenic mice. *Proc Nat Acad Sci* 94:4710-5, 1997
9. Johnatty SE, Dyck JR, Michael LH, Olson EN, Abdellatif M., Schneider M. Identification of genes regulated during mechanical load-induced cardiac hypertrophy. *J Molec Cell Cardiology* 32:805-15, 2000.
10. Nossuli TO, Lakshminarayanan V, Baumgarten G, Taffet GE, Ballantyne CM, Michael LH, Entman ML, A chronic mouse model of myocardial ischemia-reperfusion: essential in cytokine studies, *Am J Physiol - Heart Circ Physio.* 278:H1049-55, 2000.
11. Smits, JF, van Krimpen C, Schoemaker RG, Cleutjens JP, Daemen, MJ: Angiotensin II receptor blockade after myocardial infarction in rats: effects on hemodynamics, myocardial DNA synthesis, and interstitial collagen content. *J Cardiovasc Pharmacol* 20:772–778, 1992.
12. Doevendans PA, Daemen MJ, de Muinck ED, Smits JF: Cardiovascular phenotyping in mice. *Cardiovas Res* 39:34-49, 1998
13. LeGrice IJ, Smaill BH, Chai LZ, Edgar SG, Gavin JB, Hunter PJ: Lamina structure of the heart: ventricular myocyte arrangement and connective tissue architecture in the dog. *Am J Physiol Heart Circ Physiol* 269(2Pt2):H571–82,1995.
14. Basser PJ, Mattiello J, Bihan DL: MR diffusion tensor spectroscopy and imaging. *Biophys J* 66:259–67, 1994.

15. Hsu EW, Muzikant AL, Matulevicius SA, Penland RC, Henriquez CS.:Magnetic resonance myocardial fiber-orientation mapping with direct histological correlation. *Am J Physiol Heart Circ Physiol* 274:H1627–34,1998.
16. Scollan DF, Holmes A, Winslow R, Forder J: Histological validation of reconstructed myocardial microstructure obtained from diffusion tensor magnetic resonance imaging. *Am J Physiol Heart Circ Physiol* 275 44:H2308–18,1998.
17. Tung L: A bidomain model for describing ischemic myocardial D.C. potentials Ph.D. thesis. Cambridge, MA: Massachusetts Institute of Technology, 1978.
18. Henriquez CS: Simulating the electrical behavior of cardiac tissue using the bidomain model. *Crit. Rev. Biomed. Eng.* 21:1–77,1993.
19. Colli Franzone P, Guerri L, Taccardi B: Spread of excitation in a myocardial volume: Simulation studies in a model of anisotropic ventricular muscle activated by point stimulation. *J Cardiovasc Electrophys* 4:144-160, 1993.
20. Henriquez, CS, Muzikant AL, Smoak CK: Anisotropy, Fiber Curvature and Bath Loading Effects on Activation in Thin and Thick Cardiac Tissue Preparations: Simulations in a Three Dimensional Bidomain Model. *J Cardiovasc Electrophys*, 7:424-444, 1996.
21. Harrild, DM, Penland RC, Henriquez CS: A Flexible Method for Simulating Cardiac Conduction in Three-Dimensional Complex Geometries *J. Electrocardiology*, 33: 241-251, 2000.

22. Penland RC, Harrild DM, Henriquez CS: Modeling Impulse Propagation and Extracellular Potential Distributions in Anisotropic Cardiac Tissue Using a Finite Volume Element Discretization. *Comput Visual Sci*, 4:215-226,2002 .
23. Clancy C, Rudy Y: Linking a genetic defect to its cellular phenotype in a cardiac arrhythmia. *Nature* 400:566–69 1999.
24. Nerbonne JM, Nichols CG, Schwarz TL, Escande D. Genetic manipulation of cardiac K(+) channel function in mice: what have we learned, and where do we go from here?. *Circ Res* 89:944-56, 2001
25. Knollmann BC, Katchman AN, Franz MR: Monophasic action potential recordings from intact mouse heart: validation, regional heterogeneity, and relation to refractoriness. *J Cardiovas Electrophys* 12:1286-94, 2001.
26. Pandit SV, Clark RB, Giles WR, Demir SS: A mathematical model of action potential heterogeneity in adult rat left ventricular myocytes. *Biophys J* 81:3029-3051, 2001.
27. Johnson C, Parker S, Weinstein D, Heffernan S: Component-based, problem-solving environments for large-scale scientific computing. *Concurrency and Computation: Practice and Experience* 14: 1337-1349, 2002.
28. Pormann J: A Modular Simulation System for the Bidomain Equations (PhD). Durham, NC: Duke University, 1999.

29. Wikswo JP Jr., Lin SF, Abbas RA: Virtual electrodes in cardiac tissue: a common mechanism for anodal and cathodal stimulation. *Biophys J* 69:2195-2210, 1995
30. Nygren A, Clark RB, Belke DD, Kondo C, Giles WR, Witkowski FX: Voltage-sensitive dye mapping of activation and conduction in adult mouse hearts. *Ann Biomed Eng* 28:958-67, 2000.
31. Taccardi B, Macchi E, Lux, RL, Ershler, PR, Spaggiari S, Baruffi, S, Vyhmeister Y: Effect of myocardial fiber direction on epicardial potentials. *Circ* 90:3076-3090, 1995.
32. Macchi E, Cavalieri M, Stilli D, Musso E, Baruffi S, Olivetti G, Ershler PR, Lux RL, Taccardi B: High-density epicardial mapping during current injection and ventricular activation in rat hearts. *Am J Physiol Heart Circ Physiol* 275(5 Pt 2):H1886-97, 1998.
33. Muzikant AL, Hsu E, Wolf, PD, Henriquez CS: Region specific modeling of cardiac muscle: comparison of simulated and experimental potentials, *Ann Biomed Engr*, 30:867-883,2002.
34. Sampson KJ, Henriquez CS: Simulation and prediction of functional block in the presence of structural and ionic heterogeneity. *Am J Physiol: Heart Circ Physiol*, 281:H2597-H2603, 2001.
35. Lorange M, Gulrajani RM: A computer heart model incorporating anisotropic propagation. I. Model construction and simulation of normal activation. *Journal of Electrocardiology*. 26:245-61, 1993.
36. Miller, WT, Geselowitz, DB: Simulation studies of the electrocardiogram. I. The normal heart. *Circ Res* 43:301-15, 1978.

37. Berenfield, O, Jalife, J: Purkinje-Muscle Reentry as a mechanism of polymorphic ventricular arrhythmias in a 3-dimensional model of the ventricles. *Circ Res* 82:1063–1077, 1998.
38. Hren R, Nenonen J, Horacek, BM: Simulated epicardial potential maps during paced activation reflect myocardial fibrous structure. *Ann Biomed Eng.* 26:1022-35, 1998.
39. A.V.Panfilov,"Three dimensional wave propagation in mathematical models of ventricular fibrillation", in the book"Cardiac Electrophysiology. From cell to bedside", Saunders Company,Ed.D.P. Zipes and J. Jalife, 3rd edition,p.271-276,1999
40. Vigmond EJ. Ruckdeschel R. Trayanova N: Reentry in a morphologically realistic atrial model. *J Cardiovasc Electrophys.* 12:1046-54, 2001.
41. Fenton, F, Karma, A: Vortex Dynamics In 3D Continuos Myocardium With Fiber Rotation: Filament Instability and Fibrillation. *CHAOS* 8:20-65,1998.
42. McLean M, Prothero J: Myofiber orientation in the weanling mouse heart. *Am J Anat.* 192:425-41, 1991.
43. Holmes AA, Scollan DF, Winslow RL, Direct histological validation of diffusion tensor MRI in formaldehyde-fixed myocardium. *Mag Res Med.* 44(1):157-61, 2000.
44. Scollan DF. Holmes A. Zhang J. Winslow RL. Reconstruction of cardiac ventricular geometry and fiber orientation using magnetic resonance imaging. *Ann Biomed Engin* 28:934-44, 2000.
45. Noble D: Modeling the heart--from genes to cells to the whole organ. *Science.* 295:1678-1682, 2002

46. Jalife J, Morley GE, Vaidya D: Connexins and impulse propagation in the mouse heart. *J Cardiovas Electrophys* 10:1649-1663, 1999.
47. Anumonwo JMB, Tallini YN, Vetter FJ, Jalife J: Action potential characteristics and arrhythmogenic properties of the cardiac conduction system in the murine heart. *Circ Res* 89: 329-335, 2001.
48. Mahmood U, Tung CH, Tang Y, Weissleder R: Feasibility of in vivo multichannel optical imaging of gene expression: experimental study in mice. *Radiology* 224:446-51, 2002.

Figure Captions

Figure 1: Construction of the computational grid of the mouse ventricle from magnetic resonance (MR) images. A) Volume rendering of a region of the mouse ventricles from baseline MR image. B) Discrete, stair-step grid obtained from segmentation of MR image. Surface fiber directions estimated from diffusion tensor imaging (DTI) are shown as short white lines

Figure 2: Two views of heart geometry showing smooth, transmural fiber rotation in the mouse heart as estimated from DTI measurements.

Figure 3: Epicardial transmembrane and extracellular potential distributions at four time steps arising from an epicardial extracellular stimulation. During the stimulus (top row), the transmembrane potential reveals a virtual cathode with a depolarized zone adjacent to two hyperpolarized zones (V_m colormap range: -81 mV to -79 mV, isolines at -80.7 mV, -80.3 mV, -80 mV; Φ_e colormap range: -4 mV to 4 mV, isolines at -8 mV, -1 mV, and 0 mV). After the stimulus (bottom three rows), the wavefront propagates anisotropically from the stimulus site with a conduction velocity of xx cm/sec long fibers and xx cm/sec across fibers. The extracellular potential distribution is characterized by a central, elliptical negative region flanked by two regions of positivity that form along the epicardial fiber directions (V_m colormap range: -80 mV to 40 mV, isolines at -80 mV, 60 mV, -20mV, 0 mV, 20 mV; Φ_e colormap range: -2 mV to 1.8 mV, isolines at -8 mV, -2 mV, -1 mV, 0.3 mV, 0.5 mV and 1.0 mV).

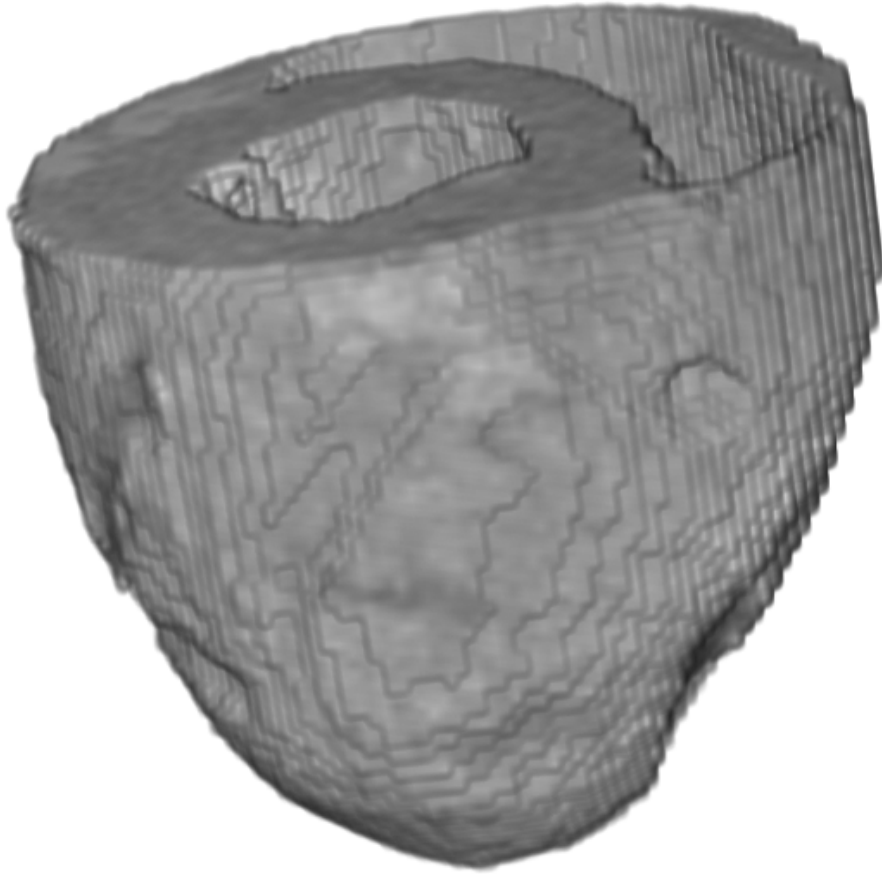
Figure 4: Isocontours of (A) activation time, (B) recovery time and (C) action potential duration (APD). The activation time is determined by tracking the time at which the potential reaches xx mV on the upstroke while the recovery time is determined by tracking the time the potential

reaches xx mV after the peak. The activation isochrones move outward from the stimulus site. Isochrones are shown every 3 msec from the range 5 msec to 23 msec. The recovery proceeds in the same direction as activation except near the stimulus (bullseye region) , where it proceeds inward so that the stimulus site is the last to recover. Isochrones are shown at 62.5 msec, 63 msec, 64 msec, 65 msec, 66 msec, 67 msec. Finally the APD is shown with the longest APD near the stimulus. Isochrones are shown every 2 msec from 43 msec to 63 msec.

Figure 5: Representative timecourses of epicardial transmembrane and extracellular potentials for a single beat, along and across fibers. The amplitude and shape of the action potential is relatively independent of direction, while the electrograms are smaller and less symmetric across fibers than along fibers. The electrograms exhibit a J-wave, coinciding with the rapid early phase of repolarization, followed by a T-wave associated with the late phase of repolarization.

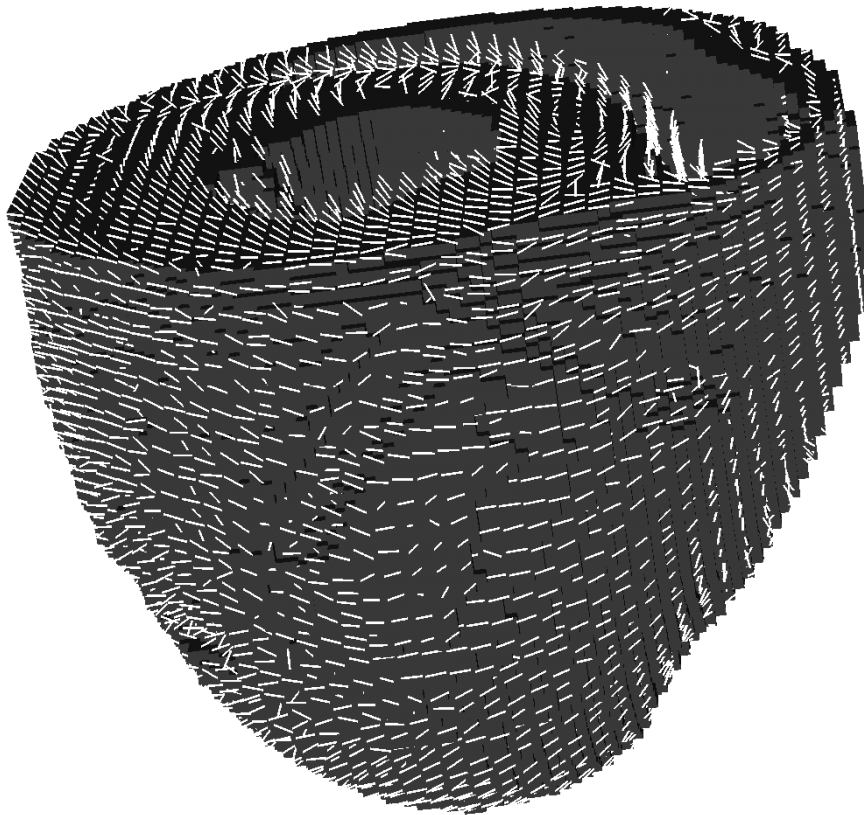
Figure 6: Time course of transmembrane potentials and electrograms during depolarization, along and across fibers at 5 sites for propagation across the wall. As the front propagates from epicardium to endocardium, there is a shift of the time corresponding to the maximum negative deflection of the extracellular potential and the maximum rate of rise of the transmembrane potential. In addition to the time shift, there is a slight increase in amplitude of the extracellular potential as the front approaches the endocardial surface.

A

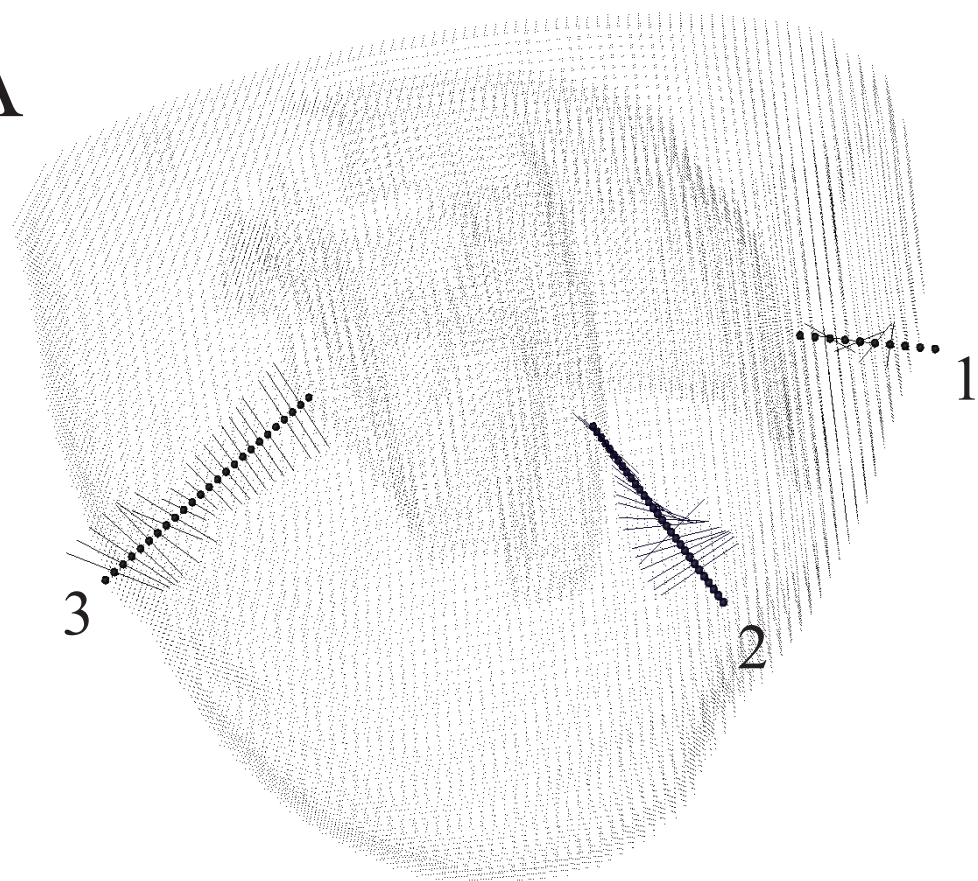


2mm

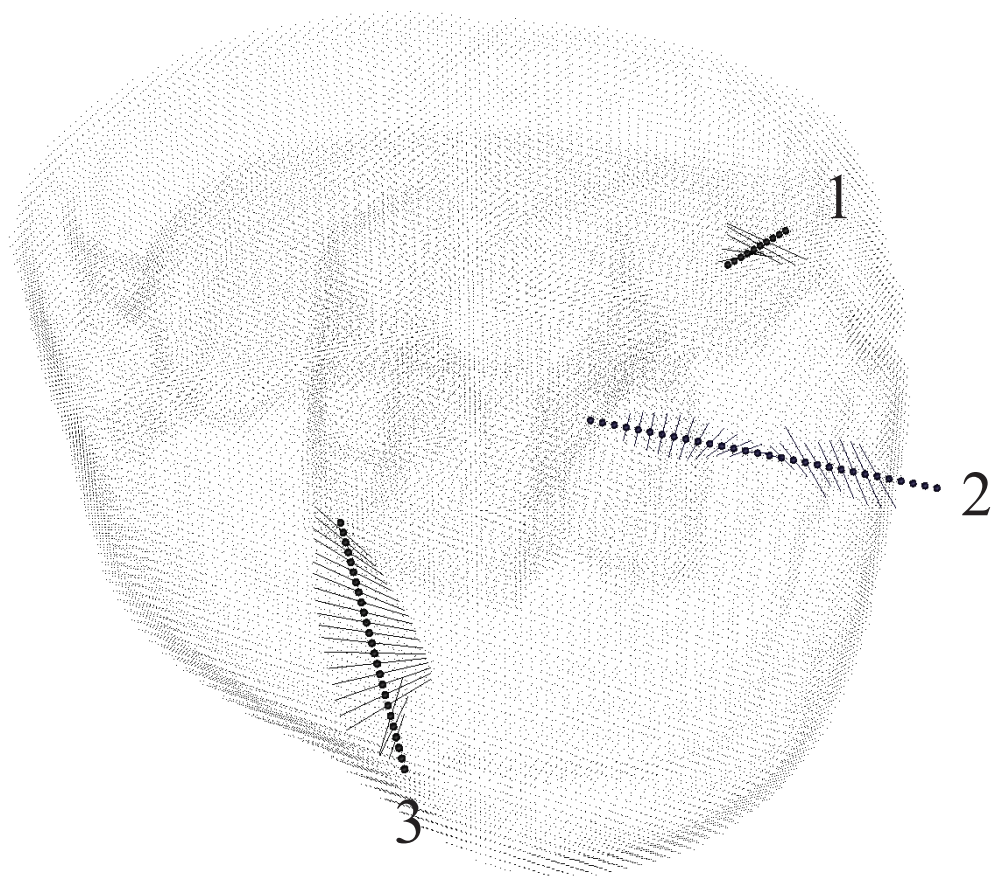
B



A



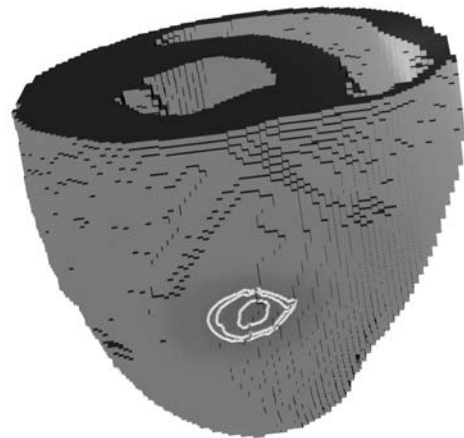
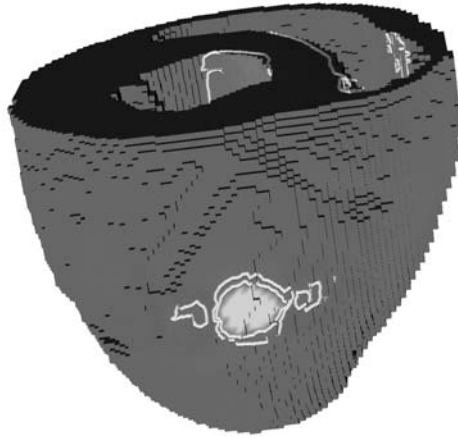
B



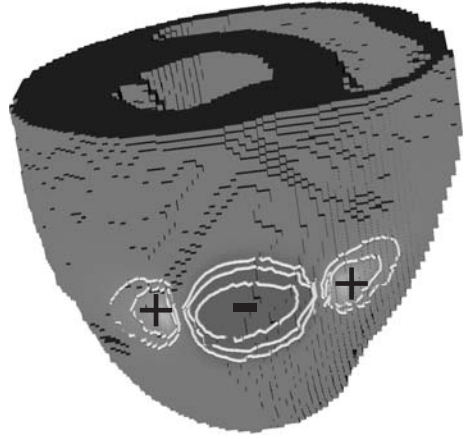
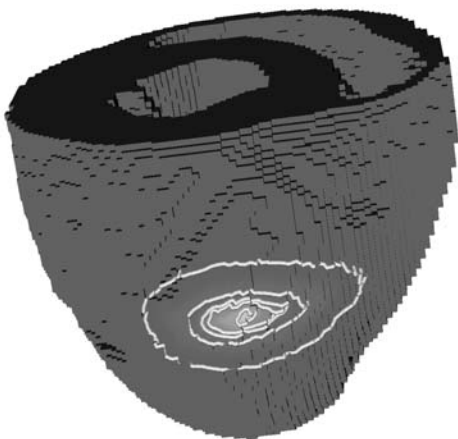
V_m

ϕ_e

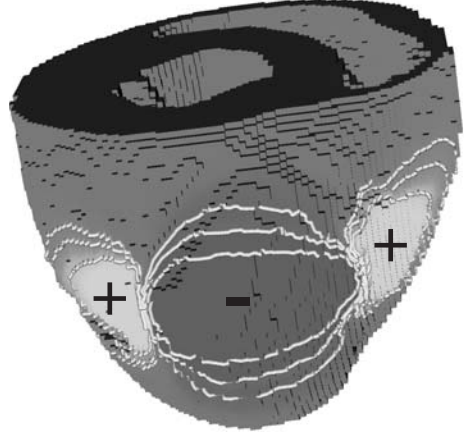
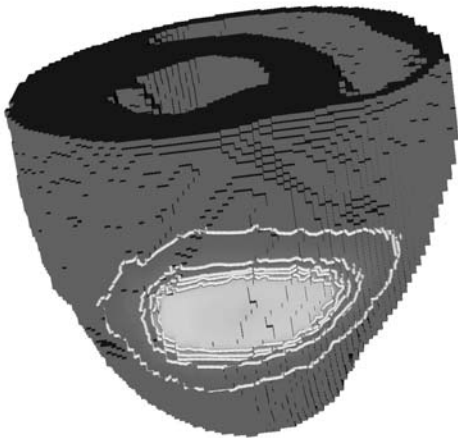
0.5ms



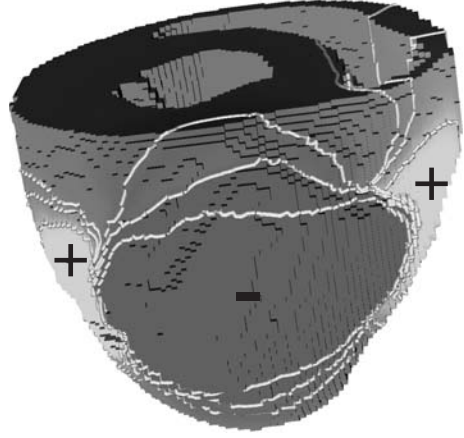
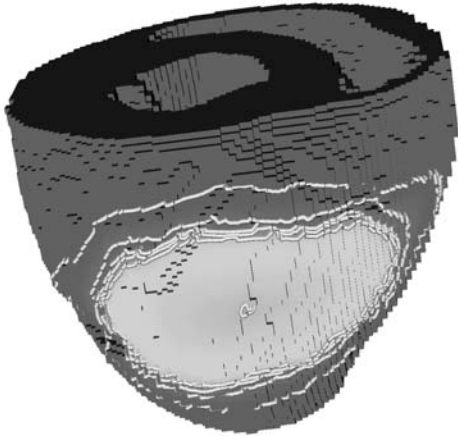
6.5ms



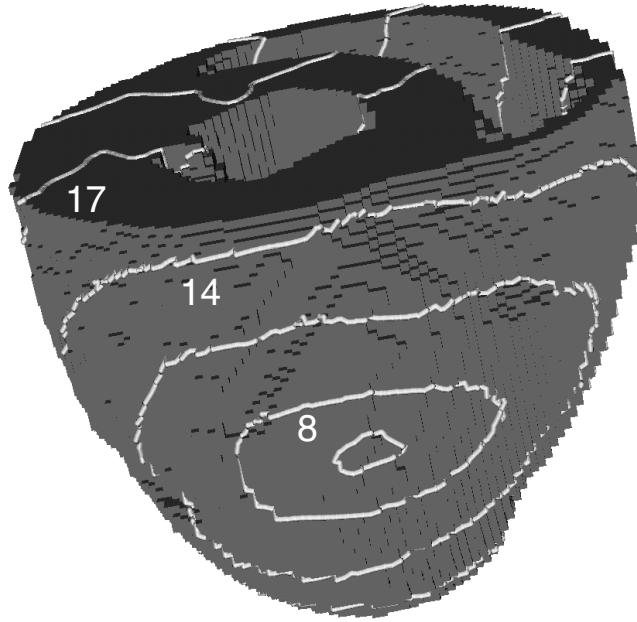
8.5ms



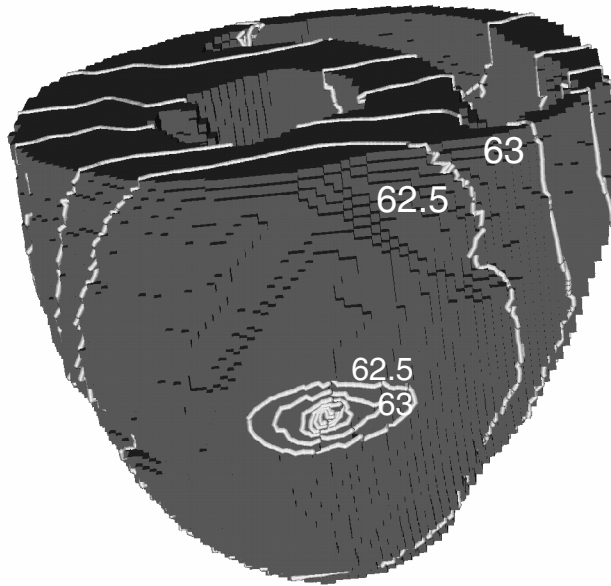
10.5ms



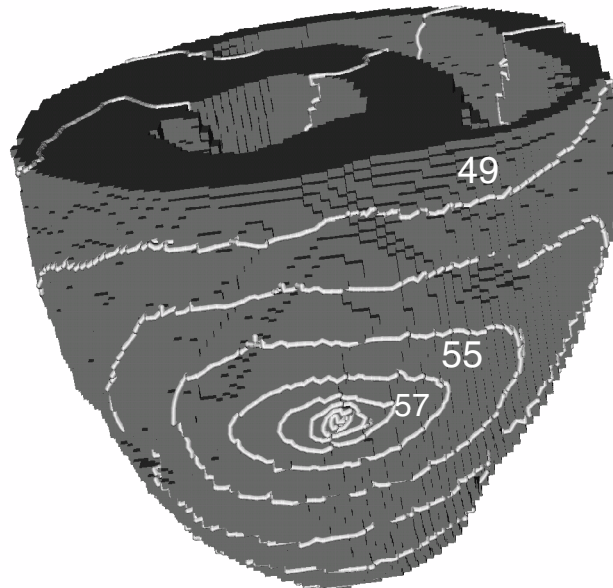
A



B



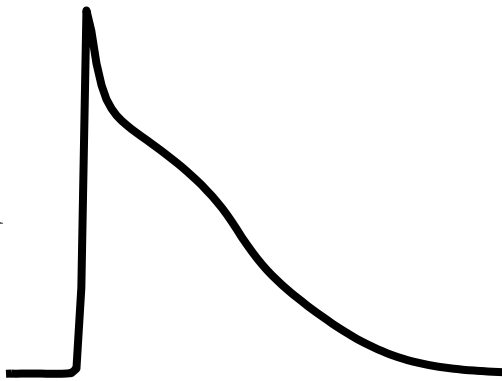
C



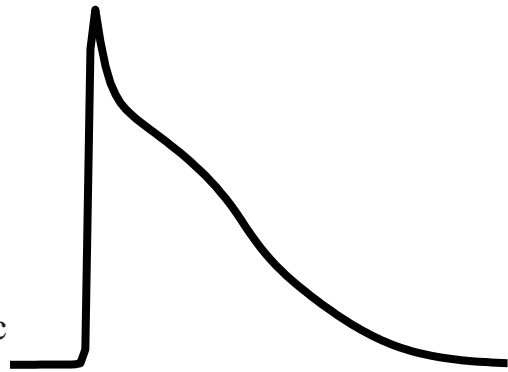
Along

Across

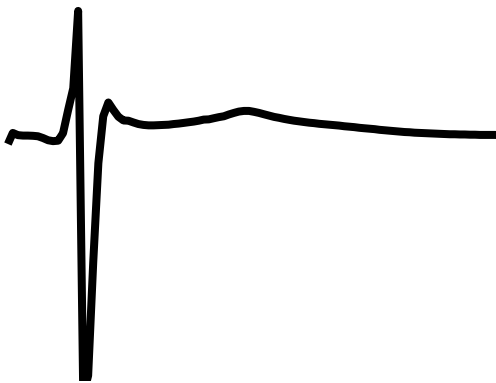
V_m



20mV
10 msec



ϕ_e



10mV
10 msec

